Available online at www.sciencedirect.com

ScienceDirect

journal homepage: www.elsevier.com/locate/he

Conical-shaped foam reactors for catalytic partial oxidation applications

Jorge E.P. Navalho, José M.C. Pereira, José C.F. Pereira*

Universidade de Lisboa, Instituto Superior Técnico, Mechanical Engineering Department, LASEF, Av. Rovisco Pais 1, 1049-001 Lisbon, Portugal

ARTICLE INFO

Article history:
Received 18 August 2013
Received in revised form
13 November 2013
Accepted 16 December 2013
Available online 25 January 2014

Keywords:
Catalytic partial oxidation
Conical-shaped reactors
Foam monolith reactors
Radiative heat transfer
Catalyst thermal stability
Methane

ABSTRACT

The role of the reactor geometry for catalytic partial oxidation of methane is numerically investigated to improve catalyst thermal stability and at the same time to achieve high fuel conversion and reforming efficiency. The performance of cylindrical-shaped foam monolith reactors is compared with that of conical-shaped foam monolith reactors. A quasi-1D heterogeneous mathematical model was developed to account for a variable reactor cross-sectional area and for a variety of chemical and transport steps. Radiative heat transfer within the cellular structure was properly accounted for with the zone method. The results suggest that converging conical-shaped reactors allow a significant decrease of the maximum surface temperatures and high reforming performance.

1. Introduction

Catalytic partial oxidation (CPOx) of hydrocarbons is a strategy to obtain synthesis gas (a mixture composed mainly by H_2 and CO) through the application of specific catalyst formulations, supports, reactor configurations and proper operating conditions. Literature work on this field has been gaining interest over the last twenty years after the pioneering work carried out by Schmidt and co-workers [1,2]. Catalytic partial oxidation of hydrocarbons has been considered suitable for a large number of applications ranging from small- to medium-scale fuel pre-processor units for on-board and stationary fuel cell systems to the production of bulk chemicals, namely H_2, ammonia, methanol and even liquid hydrocarbons through the Fischer–Tropsch synthesis [3].

The packed bed reactor, the honeycomb monolith and the foam monolith reactor are the most widespread reactor types employed for catalytic partial oxidation. The choice of the catalyst support structure is usually dependent on the intended application. A general agreement exists concerning the most active catalyst materials for performing catalytic partial oxidation: platinum group metals (except Os) are widely assumed as the most active catalysts but their high prices make them unattractive and often they are replace by other inexpensive transition metals such as Ni [3]. Among the platinum group metal catalysts Rh stands out as the noble metal that offers the highest activity and syngas selectivity

* *Corresponding author*. Tel.: +351 218417928.
E-mail addresses: jorge.navalho@tecnico.ulisboa.pt (J.E.P. Navalho), jose.chaves@tecnico.ulisboa.pt (J.M.C. Pereira), jcfpereira@tecnico.ulisboa.pt (J.C.F. Pereira).

0360-3199/$ – see front matter
http://dx.doi.org/10.1016/j.ijhydene.2013.12.107

Nomenclature

A	area; reactor cross-sectional area, m^2
A_{Ri}	pre-exponential factor in the rate coefficient of the reaction Ri
C_p	specific heat capacity at constant pressure, J kg^{-1} K^{-1}
D_p	mean pore diameter, m
$F_{cat/geo}$	ratio of the catalytic surface to the total geometric surface area
H_k	molar enthalpy of species k, J mol^{-1}
KK	total number of species
$K_{mat,k}$	interphase mass transport coefficient of species k, m s^{-1}
L	length, m
LHV	low heating value, J kg^{-1}
N_g	total number of volume zones
N_s	total number of surface zones
P	operating pressure, Pa
R	universal gas constant, J mol^{-1} K^{-1}
Re	Reynolds number
S_{CO}	carbon monoxide selectivity
S_{H_2}	hydrogen selectivity
Sc	Schmidt number
Sh	Sherwood number
T	temperature, K
T_{rad}	exchange temperature, K
V_k	diffusion velocity of species k, m s^{-1}; volume of zone k, m^3
W	molecular weight, kg mol^{-1}
X_{CH_4}	methane conversion
Y_k	mass fraction of species k
$\dot{V}_{total}$	total volumetric flow rate, m^3 s^{-1}
$\dot{n}$	molar flow rate, mol s^{-1}
$\overline{Z_iZ_j}$	total exchange area between (surface − S − or volume − G) zones i and j, m^2
a_V	specific surface area, m^{-1}
d	internal reactor diameter, m
h	interphase heat transport coefficient, W m^{-2} K^{-1}
k	thermal conductivity, W m^{-1} K^{-1}
q'''_{rad}	net radiative heat flux, W m^{-3}
q_{loss}	radiative heat loss, W
t	time, s
u	axial (interstitial) mean flow velocity, m s^{-1}
x	axial reactor coordinate, m

Greek letters

β	extinction coefficient, m^{-1}
β_{Ri}	temperature exponent in the rate coefficient of the reaction Ri
$\dot{\omega}_k$	net molar production/consumption rate of species k due to surface reactions, mol m^{-2} s^{-1}
ε	porosity
ε_i	emissivity of surface zone i
η_{ref}	reforming efficiency
Γ	surface site density, mol m^{-2}
γ_{Ri}	sticking coefficient of the adsorption reaction Ri
κ_i	absorption coefficient of volume zone i, m^{-1}
λ	air to fuel equivalence ratio
Ω	relative radiative heat losses
ω	single scattering albedo
ρ	density, kg m^{-3}
σ	Stefan–Boltzmann constant, W m^{-2} K^{-4}; site occupancy number
τ	solid tortuosity factor
θ_k	surface coverage of species k

Subscripts

cat	catalyst
g	gas phase; gas species
g_i	volume zone i
k	species k
s	solid phase; surface (adsorbed) species
s_i	surface zone i
w	wall species

Superscripts

in	inlet
out	outlet

producing at the same time the lowest levels of carbon deposits [4,5].

Catalytic partial oxidation has been widely studied and explored in the literature through the application of numerical modeling tools. Several mathematical models have been proposed to model the performance of catalytic partial oxidation reactors ranging from pseudo-homogeneous and heterogeneous 1D single-channel models (lumped models in the radial and angular directions) to 2D multi-channel continuum or discrete models [6–10]. In particular, 1D heterogeneous models are largely employed due to their relative good compromise between predictive capability and computational cost requirements. This class of models allows for fast reactor performance predictions being largely preferred for parametric investigations in early reactor design stages [10].

For methane catalytic partial oxidation several reliable reaction mechanisms have been proposed in the literature. The first detailed description on the reaction kinetics of methane CPOx over noble metals (Rh and Pt) in high temperature simulations was performed by Hickman and Schmidt [11]. For Rh-based catalysts, improved versions of the earlier mechanism were developed by Deutschmann and co-workers for stationary and transient kinetic studies [9,12]. Other kinetic schemes have been reported for methane CPOx over Rh catalysts such as the molecular indirect and consecutive reaction mechanisms described through Langmuir–Hinshelwood kinetic expressions developed by Tavazzi et al. [13] and Donazzi et al. [14] or the 104-step C_1 microkinetic scheme developed by Mhadeshwar and Vlachos [15] that was further enhanced by Maestri et al. [16] for the particular case of methane conversion to syngas and hydrogen on Rh/Al_2O_3 catalysts resulting in a microkinetic scheme composed by 82 elementary reactions.

A consensual issue that concerns a broader application (intensification) of catalytic partial oxidation is the catalyst thermal stability and thermal management in the reactor [17–19]. Specific regimes of reactor operation, for instance high total flow rates and high preheating temperatures, may lead to very high surface temperatures (hot spots) in particular near the catalyst entrance region of a fresh catalyst sample [17,20]. These high surface temperatures inside the catalyst bed may trigger thermal deactivation mechanisms through a reduction of the active surface area that rapidly lead to a significant loss of catalyst activity and selectivity conducting to the catalyst disposal. Metal sintering and catalyst support/carrier phase transformations are considered the major causes towards a reduction in the catalytic surface area of supported catalysts [21].

Several works have reported a progressive catalyst aging after catalyst exposure to very high temperatures during partial oxidation of methane. An irrefutable sign of catalyst degradation is the modification of the catalyst thermal behavior for a constant operating condition as the time-on-stream increases. Concerning catalytic partial oxidation of methane over Rh/Al_2O_3 coated spheres in a packed bed reactor, Tavazzi et al. [22] have found an increase in the maximum temperatures as well as a progressive shift in their location towards the reactor outlet. A delay in the deactivation phenomena at the reactor outlet was observed: although the catalyst had already effective signs of deactivation in specific reactor locations, at integral conditions no signs of deactivation were detected. Similar findings for the axial temperature distribution were also reported for Rh-based honeycomb structured catalysts by Beretta et al. [17] under extremely severe operating conditions. The authors stressed that measurements of reactor performance at the exit section did not constitute any piece of evidence on the complete integrity of the catalyst bed (absence of deactivation). The observed increase in the maximum surface temperatures near the catalyst inlet section was explained through numerical analysis by a progressive decrease along the flow direction of the overlay between exothermic (O_2-driven) and endothermic (CH_4-driven) reactions since O_2 consumption is fully governed by external transport and then highly insensitive to a decrease in the metal surface area while CH_4 reforming reactions are markedly affected by a loss of catalyst surface area. They also observed an increase in the light-off temperature (ignition delay) as the deactivation progressed. With respect to Rh-coated foam catalysts, Ding et al. [23] reported for a 1000 h experiment that significant sintering of the active phase in the catalyst entrance region was the main cause for catalyst deactivation. They observed during the course of the experiment a slight decrease of integral methane conversion and H_2 selectivity as well as an increase in the catalyst outlet temperature.

Several strategies have been proposed and somewhat explored in the literature by numerical and experimental means to decrease the hot spot temperature that establishes near the catalyst entrance section in such a way that catalyst thermal stability and heat management are improved contributing for a long term catalyst operation (longer durability). Among the most explored techniques are the addition to the reactor feedstock of oxidizing agents, such as CO_2 and H_2O to promote endothermic reforming reactions and decrease reactor temperatures [23,24], addition (dilution) of inert species with high specific heat [23,24], tunning reactor thermophysical [19,25] and geometrical properties [18,23], tunning catalyst loading [18,23] and improving catalyst formulations [26]. In a recent work Livio et al. [27] have experimentally explored the purposeful effect of operating with lower reactor thermal efficiencies by separating or removing the radiation shield upstream the catalyst bed. Significant decreases of the hot spot temperature were registered in particular for the absence of the front heat shield. Such findings have been corroborated by Navalho et al. [28] through an extensive numerical analysis on the performance of non-adiabatic honeycomb monolith reactors. Other explored strategies to decrease surface temperatures have been also proposed based on the method employed to supply the oxygen stream into the reactor: (1) slipping the oxygen stream in specific axial positions [6,29] or (2) supplying the oxygen stream gradually along the reactor length through oxygen-permeable membranes [29–32]. Both strategies aim to distribute the oxygen feed stream along the reactor main flow direction in such a way that the overlapping between endothermic and exothermic reactions is promoted resulting in milder reactor temperatures.

In the large majority of literature works on catalytic partial oxidation carried out with foam catalysts the reactor has a cylindrical-shaped geometry. The frontal open flow area and catalyst volume are generally tailored to achieve high integral reforming performance and catalyst stability under a specific range of operating conditions (inlet mixture composition, flow rate, gas temperature and pressure). However, to attain a reasonable high reforming performance over the whole operating spectrum very high surface temperatures may be experienced as the limits of the operating range are reached.

Little attention has been paid in literature to the geometrical configuration of foam monolith reactors employed for catalytic partial oxidation. Therefore, the present paper aims to investigate the role of the foam monolith geometrical configuration, namely as a route to improve catalyst thermal stability and at the same time to obtain high reforming performance.

The paper is structured as follows. In the next section the reactor geometries and thermophysical properties are presented followed by the introduction of the quasi-1D model equations, the thermal radiation method and underlying details related to external heat and mass transport phenomena as well as the surface chemistry formulation. Boundary conditions to close the boundary value problem are also conveniently presented. Section 3 presents the results for the different geometrical configurations under several operating conditions and Section 4 closes the paper with summary conclusions.

2. Modeling

2.1. *Reactor geometries and thermophysical properties*

Three reactor configurational shapes were considered to conduct this study (see Fig. 1). The cylindrical configuration

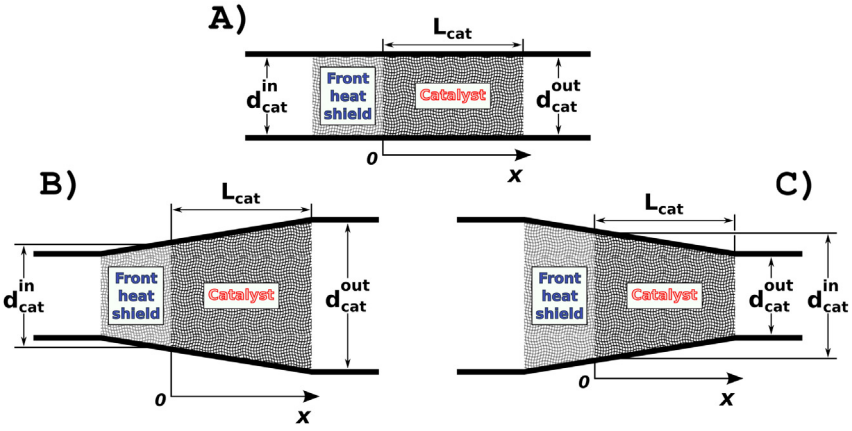

Fig. 1 – Geometrical configurations considered for the foam reactor.

was considered with three different diameters (herein referred to as cases A1), A2) and A3)) while the two remaining case studies are related to conical-shaped geometries (cases B) and C) – see Fig. 1). The geometrical parameters (d_{cat}^{in}, d_{cat}^{out} and L_{cat}) for each foam reactor configuration (case study) can be found in Table 1. In order to provide a valid comparison between the performance accomplished in each case study the catalyst volume is kept constant for all case studies and therefore the catalyst length (L_{cat}) varies from case study to case study. For all case studies a heat shield was applied prior to the catalyst bed in order to avoid heat losses by radiation from the reactor. The front heat shield length was held constant at 1.0 cm for all reactor geometries. The cylindrical-shaped foam reactor assigned to the case study A1) is the reference geometrical configuration.

For all reactor configurations 45 ppi α–Al_2O_3 foams were considered for the heat shield and catalyst support. The catalyst region comprises a thin Rh/Al_2O_3 washcoat layer in such a way that the geometrical and thermophysical properties of uncoated and washcoated foams are considered equal. Tables 2 and 3 present the geometrical parameters and thermophysical properties of the reticulated structures.

conductivity of α-alumina was taken as a function of the solid temperature as suggested in Ref. [33] and the radiative properties for the present foam type were collected from Ref. [36]. The internal ring-shaped surface that encases the foam structures in place is assumed to be a perfectly reflective surface by a zero-valued emissivity.

2.2. *Governing equations*

The transport equations herein considered are based on a 1D heterogeneous mathematical model for a fixed bed reactor (see Refs. [28,37]). The model accounts for energy and species mass balances in the bulk gas flow phase and in the solid phase. A large variety of chemical and transport steps are embraced by the mathematical model by employing reliable heat transfer models and correlations, catalytic reaction steps and constitutive relations. The gas phase reactor performance is governed by quasi-1D equations, Equations (1) and (2) that state the species profiles and gas temperature, respectively. The species composition at the bulk gas/washcoat external interface and the solid thermal profile are dictated by Equations (3) and (4), respectively.

$$A\varepsilon\rho_g\frac{\partial Y_{k,g}}{\partial t}+A\varepsilon\rho_g u\frac{\partial Y_{k,g}}{\partial x}+\frac{\partial}{\partial x}\left(A\varepsilon\rho_g Y_{k,g}V_{k,g}\right)+Aa_V\rho_g K_{mat,k}\left(Y_{k,g}-Y_{k,w}\right)=0 \quad (1)$$

$$A\varepsilon\rho_g C_{p,g}\frac{\partial T_g}{\partial t}+A\varepsilon\rho_g uC_{p,g}\frac{\partial T_g}{\partial x}-\frac{\partial}{\partial x}\left(A\varepsilon k_g\frac{\partial T_g}{\partial x}\right)+A\varepsilon\rho_g\sum_{k=1}^{KK_g}C_{p,k}Y_{k,g}V_{k,g}\frac{\partial T_g}{\partial x}+Aa_V h\left(T_g-T_s\right)=0 \quad (2)$$

$$-a_V\rho_g K_{mat,k}\left(Y_{k,g}-Y_{k,w}\right)-a_V F_{cat/geo}\dot{\omega}_{k,w}W_k=0 \quad (3)$$

$$A(1-\varepsilon)\rho_s C_{p,s}\frac{\partial T_s}{\partial t}-\frac{\partial}{\partial x}\left(A\tau k_s(1-\varepsilon)\frac{\partial T_s}{\partial x}\right)-Aa_V h\left(T_g-T_s\right)+Aa_V F_{cat/geo}\sum_{k=1}^{KK_w}\dot{\omega}_{k,w}H_k+Aq'''_{rad}=0 \quad (4)$$

The geometrical properties of the cellular structures were obtained from the experimental and theoretical work reported in Ref. [34], the solid tortuosity factor was estimated based on the correlation provided in Ref. [35], the intrinsic solid thermal

In this study gas phase reactions were not considered due to the negligible homogeneous conversion route of reactants and intermediate species during catalytic partial oxidation of methane at atmospheric pressure and typical

Table 1 – Geometrical parameters of the foam reactor configuration for each case study.

Case study	d_{cat}^{in}[cm]	d_{cat}^{out}[cm]	L_{cat} [cm]
A1)	1.70	1.70	2.00
A2)	2.20	2.20	1.19
A3)	2.70	2.70	0.79
B)	1.70	2.70	1.17
C)	2.70	1.70	1.17

feed conditions [12,18]. The momentum balance equation was not accounted for in the model scheme since the pressure drop along the reactor is generally neglected from the thermodynamic standpoint [8,19,37]. The gas phase species mass balance equation (Equation (1)) was applied to all species and due to the molecular diffusion inclusion through the mixture-averaged formalism a corrective procedure to assure the overall mass conservation was applied based on the corrective diffusion velocity approach (see Ref. [38]). Thermal diffusion due to the Soret effect was included as well in the molecular diffusion. External mass transport coefficients were evaluated through a suitable Sherwood correlation (Equation (5)) for the considered foam structure and operating conditions [34].

$$Sh_k = Re^{0.47} \cdot Sc_k^{1/3} \cdot \left(\frac{D_p[m]}{0.001}\right)^{0.58} \cdot \varepsilon^{0.44} \tag{5}$$

The Chilton–Colburn analogy was considered for evaluation of the local Nusselt value for further determination of the convective heat transfer coefficient, h.

The surface chemistry was accounted for through the detailed reaction mechanism developed by Deutschmann and co-workers for methane oxidation on Rh coated Al_2O_3 catalysts [39]. This reaction mechanism comprises 38 elementary and irreversible reaction steps, 6 reactive gas phase species and 11 surface species. The role of steam reforming, dry reforming and water-gas shift reactions is not disregarded in the overall kinetic scheme. Even though improved versions of the present reaction mechanism have been evolved in recent years mainly to embrace transient phenomena (light-off performance) and the conversion of higher hydrocarbons [9,40] the considered kinetic model has been widely validated against experimental data and is currently in use [8,20,25].

The evaluation of the rate coefficients with the microkinetic scheme considered is based on the fact that the mean-field approach is valid assumption. This approximation states that the surface is uniform and described by its temperature and a set of surface coverages. Therefore, the rate coefficient of adsorption reactions is computed through sticking coefficients as Equation (6) shows for the particular case of reaction Ri that describes the adsorption of the species k. In Equation (6), the exponent m of the surface site density (Γ) corresponds to the sum of the stoichiometric coefficients of surface reactants in the reaction Ri (number of surface sites occupied by the adsorption of the gas phase k species).

Table 2 – Geometrical properties of the foam structure.

ε[–]	0.761
a_V[m^{-1}]	2717.859
D_p[m]	0.867×10^{-3}
τ[–]	0.50

Table 3 – Thermophysical properties of the foam structure.

k_s[W m^{-1} K^{-1}]	$f(T_s)$ (see Ref. [33])
β[m^{-1}]	776.0
ω[–]	0.70
Surface emissivities [–]	
Inlet/outlet manifold surfaces	0.15
Blank foam monoliths ends	0.70

$$k_{Ri} = \frac{\gamma_{Ri}}{\Gamma^m}\sqrt{\frac{RT}{2\pi W_k}} \tag{6}$$

Regarding surface and desorption reactions the modified Arrhenius expression is employed through Equation (7) where the parameters $\mu_{k,Ri}$ and $\varepsilon_{k,Ri}$ intend to modify the pre-exponential factor and the activation energy, respectively, due to surface coverage by species k.

$$k_{Ri} = A_{Ri} T^{\beta_{Ri}} \mathrm{Exp}\left(\frac{-E_{a,Ri}}{RT}\right) \prod_{k=1}^{KK_s} \theta_k^{\mu_{k,Ri}} \mathrm{Exp}\left(\frac{\varepsilon_{k,Ri}\theta_k}{RT}\right) \tag{7}$$

The rate-of-progress variable of each reaction, evaluated according to the law of mass action kinetics, allows to determine the net molar production/consumption rate of surface species (adsorbates) and gas phase species at the catalyst wall, $\dot{\omega}_{k,s}$ and $\dot{\omega}_{k,w}$, respectively. The net molar formation/destruction rate of adsorbed species should satisfy Equation (8) according to which at steady-state conditions the creation rate of each surface species is equal to its depletion rate.

$$\frac{d\theta_k}{dt} = \frac{\dot{\omega}_{k,s}\sigma_k}{\Gamma} \tag{8}$$

In the present work the surface site density which represents the total number of gas phase species that can be adsorbed per unit of active surface area was assumed to be equal to 2.72×10^{-9} mol cm^{-2} [9].

Mass and heat transfer limitations in the thin washcoat layer were neglected [41,42]. Moreover, the parameter $F_{cat/geo}$ (see the solid phase balance equations – Equations (3) and (4)) that accounts for surface activity due to metal dispersion and loading in the washcoat layer is considered to be equal to 10.0. This is a suitable value for such parameter taking into account a thin Rh/Al_2O_3 washcoat layer (see Refs. [40,41]).

2.3. *Radiative heat transfer model*

The porous matrix was considered as a pseudo-homogeneous medium to account for the radiative heat transport between surfaces belonging to different reactor axial positions. The radiative role of gaseous mixture is broadly acknowledged as negligible comparing to the surface–surface radiant heat exchange [43]. Continuum radiative properties along with gray and diffusive surfaces were regarded taking in consideration that the porous medium emits, absorbs and isotropically scatters radiation.

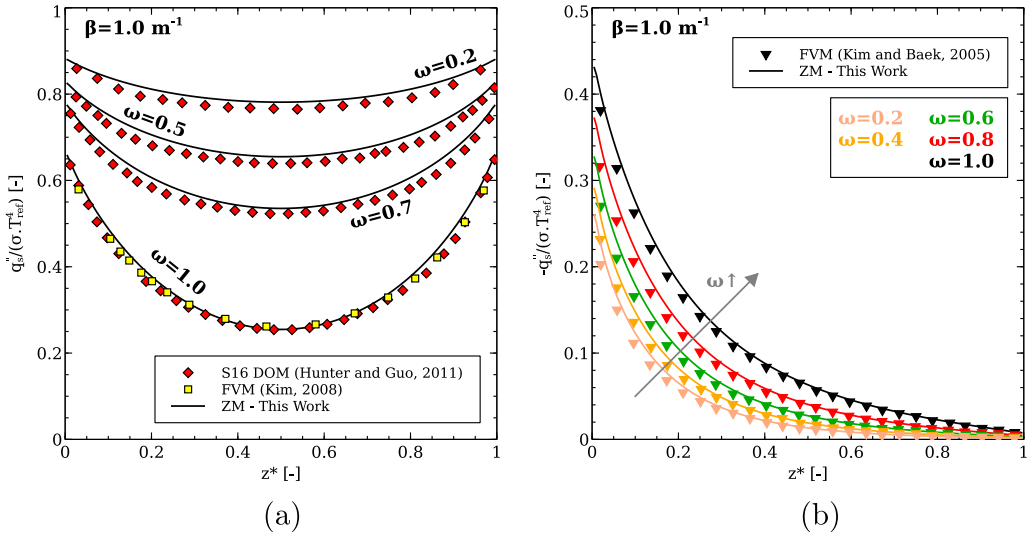

Fig. 2 – Comparison of dimensionless radial wall heat flux on the side wall for absorbing/emitting media with isotropic scattering confined in a: a) cylindrical enclosure; b) truncated conical enclosure. Radiative properties: $\beta=1.0\ m^{-1}$; ω variable.

The zone method [44] was implemented to provide the net radiative heat fluxes for each reactor cross-section. Direct exchange areas (DEAs) were calculated through direct numerical integration of four-, five- and six-fold DEAs integrals. To assure the fulfillment of conservation constraints the least-squares smoothing procedure proposed in Ref. [45] was applied to the raw direct exchange areas matrix. Total exchange areas (TEAs) that account for direct radiation between zones as well as for radiation scattered and multiple wall reflections were evaluated through the unified matrix formulation developed in Ref. [46]. Finally, the net radiative heat flux from each volume zone is evaluated through Equation (9) where T_{gi} is the temperature of the gas/volume zone i that is the temperature of the solid phase in the axial location centered in the gas/volume zone i and T_{sj} is the temperature of the surface zone j.

$$q'''_{g_i} = 4\kappa_i\sigma T^4_{g_i} - \frac{1}{V_i}\sigma\left(\sum_{j=1}^{N_s}\overline{S_jG_i}T^4_{s_j} + \sum_{j=1}^{N_g}\overline{G_jG_i}T^4_{g_j}\right) \tag{9}$$

In the present work surface zones are ring-shaped surfaces coincident with the boundaries of the foam monolith reactor and disk-shaped surfaces that close the reactor at the inlet and outlet sections. The internal ring-shaped surface that surrounds the porous medium is herein regarded as a pure reflective surface (non-participating). Furthermore, radiative heat losses through the inlet and outlet sections are considered. Therefore, the total exchange area value between surface zone j and volume zone i ($\overline{S_jG_i}$) is only different than 0 if j corresponds to one of the two disk-shaped surfaces that encloses the radiative system at the inlet and outlet sections.

2.4. Boundary conditions

For each case study considered the computational domain is made coincident with the boundaries of the corresponding physical model (see Fig. 1).

The set of governing equations constitutes a boundary value problem that is subjected to the following boundary conditions: at the inlet section Danckwerts boundary conditions are considered for species mass and energy balance equations of the gas phase (Equations (10) and (11), respectively) while for the energy balance of the solid phase a radiative boundary condition is applied (Equation (12)); at the computational domain exit section zero advective fluxes (zero-Neumann type of boundary conditions) are imposed for the balance equations of the gas phase (Equations (13) and (14)) and a radiative boundary condition is considered for the energy balance equation of the solid phase (Equation (15)).

Inlet reactor section:

$$u\left(Y_{k,g} - Y^{in}_{k,g}\right) + Y_{k,g}V_{k,g} = 0 \tag{10}$$

$$\rho_g C_{p,g} u\left(T_g - T^{in}_g\right) - k_g\frac{\partial T_g}{\partial x} = 0 \tag{11}$$

$$k_s\frac{\partial T_s}{\partial x} - \sigma\varepsilon_s\left(T^4_s - \left(T^{in}_{rad}\right)^4\right) = 0 \tag{12}$$

Outlet reactor section:

$$\frac{\partial Y_{k,g}}{\partial x} = 0 \tag{13}$$

$$\frac{\partial T_g}{\partial x} = 0 \tag{14}$$

$$k_s\frac{\partial T_s}{\partial x} + \sigma\varepsilon_s\left(T^4_s - \left(T^{out}_{rad}\right)^4\right) = 0 \tag{15}$$

2.5. Numerical model

An in-house version of the PREMIX code [47] was developed taking into account the mathematical model formulation.

Finite difference approximations are employed to reduce the boundary value problem to a system of algebraic equations following the native approach of the PREMIX code. The problem is solved through a damped Newton's method. Whenever this method fails to converge (when the solution lies out of the steady-state domain of convergence) a time-stepping procedure is applied in an attempt to bring the solution into the Newton's domain of convergence. Initially, a coarse uniform mesh is considered and after successful convergence on this mesh new grid points are continuously added to the mesh until the solution satisfies the degree of resolution for its gradients and curvatures specified by the user.

CHEMKIN correlations [48,49] are employed for the evaluation of thermodynamic and transport properties considering thermodynamic and transport coefficients supplied by GRI-Mech 3.0 database [50].

3. Results

3.1. Radiative model verification

The radiative zone method was verified against two benchmark problems regarding axisymmetric enclosures: a cylindrical enclosure and a conical frustum (truncated conical) enclosure. Both benchmarks consider radiative heat transport through an absorbing/emitting medium with isotropic scattering.

The first benchmark problem is concerned with the cylindrical enclosure with a radius of 1.0 m and a height of 2.0 m with black walls. The top and bottom walls are cold (0 K) whereas the side wall is at a constant temperature of 64.8 K ($E_b = 1.0$ W m^{-2}). The enclosed medium is cold (0 K) with a constant extinction coefficient of $\beta_g = 1.0$ m^{-1}. Four single scattering albedos are considered: $\omega_g = \{0.2;0.5;0.7;1.0\}$. Fig. 2a shows the results for the non-dimensional side wall heat flux evaluated with the present radiative model along with reference results taken from the literature (see Refs. [51,52]). A good agreement is verified denoting an appropriate implementation of the zone method for the problem in hand.

The second benchmark problem considers the truncated conical enclosure geometrically defined by a bottom and top surface radii of 1.0 and 2.155 m, respectively, and a height of 2.0 m. The enclosed medium is cold (0 K) having an extinction coefficient equal to 1.0 m^{-1}. Five different values for the single scattering albedo are considered, ranging from 0.2 to the pure scattering case - 1.0. For this benchmark study, Fig. 2b presents the reference results [53] and the results herein obtained.

A general good agreement is observed in Fig. 2a and b between the results obtained with the present thermal radiation method and the results reported in literature for the set of benchmark problems reported above.

3.2. Model validation

In this section the mathematical model considered for the description of the overall reactor performance is validated against the experimental results reported by Donazzi et al. [42]. The results are related to the autothermal catalytic partial oxidation of methane over Rh coated Al_2O_3 foam catalyst. The reactor layout is composed by a 5 wt.% Rh coated 80 ppi α–Al_2O_3 foam that is sandwiched between the front and back heat shields (uncoated 80 ppi α–Al_2O_3 foams). The experimental data was gathered through the spatially resolved sampling technique which for validation purposes allows for a detailed validation of model predictions concerning temperature and product distribution profiles along the reactor main flow direction. Thermophysical data and geometrical properties provided in Ref. [42] were herein employed. Regarding the radiative heat transfer modeling, radiative properties available in Ref. [37] were considered. To account for metal loading and metal dispersion in the kinetic rates of species production/destruction a value equal to 3.0 was considered for the $F_{cat/geo}$ parameter which is consistent with typical values encountered in the literature for similar catalyst formulations [8].

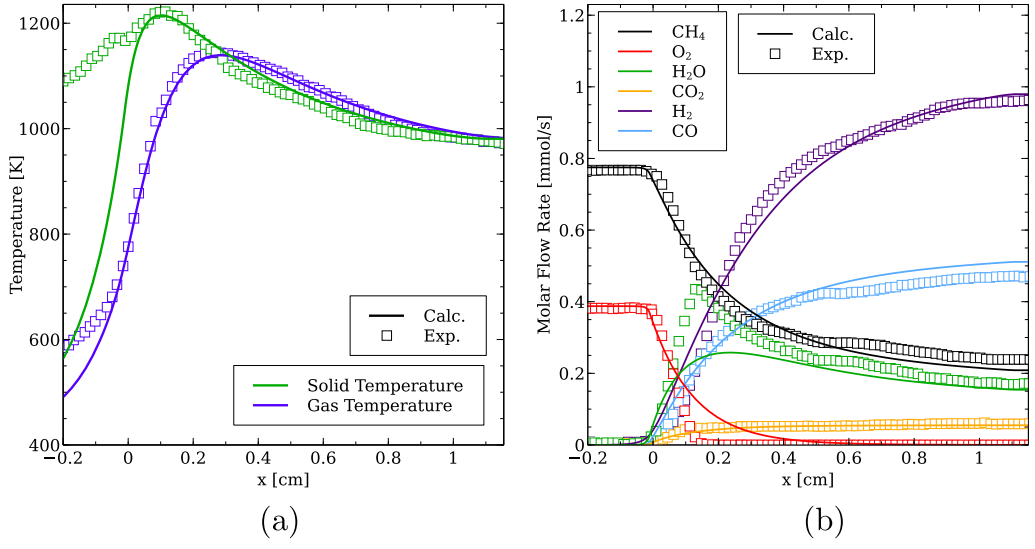

Fig. 3 – Comparison between model predictions and experimental data: a) surface and gas temperature profiles; b) product distribution profiles. Operating conditions: $\dot{V}_{total}$ = 5 slpm; λ = 0.25; 20% CH_4; Ar to balance; T_{in} = 423.15 K; P = 1 atm.

Fig. 3 shows the comparison between the results computed with the current numerical model and the reference experimental results. A good matching between the numerical and experimental temperature profiles is observed in Fig. 3a. The model is able to accurately predict the location as well as the value of the surface hot spot. Regarding the species composition profiles along the catalyst bed Fig. 3b shows that the main evolution trends are reasonably well predicted by the model.

3.3. *Effect of the reactor geometry*

To investigate the role of the reactor geometry on the overall reaction behavior a specific operating condition is considered and defined by an inlet gas temperature of 600 K, an air ratio of 0.31 (25.3% CH_4, 15.7% O_2 and 59.0% N_2) and a total volumetric flow rate of 10 NL/min. Operation at atmospheric pressure and under steady-state conditions is considered as well.

Fig. 4a shows the surface temperature profiles for the five case studies listed in Table 1. The maximum surface temperatures are attained near the catalyst entrance section independently of the reactor geometry. Fig. 4b shows the same data as Fig. 4a but as a function of the dimensionless catalyst volume.

Regarding the cylindrical-shaped reactor geometries (case studies A1), A2) and A3)), a significant decrease of the maximum surface temperatures is observed upon increasing the internal reactor diameter. For instance, a decrease in the maximum surface temperature of about 80 K occurs between case studies A1) and A3). However, an increase in the reactor cross-sectional area is equally responsible for an increase in the surface temperatures along the front heat shield (see Fig. 4a) due to a decrease in the superficial flow velocity that leads to an increasing thermal decoupling regime between gas and solid phases. This increase in surface temperatures along the front heat shield can ultimately decrease the overall reactor thermal efficiency [7]. Nevertheless, for the operating condition considered in Fig. 4 the relative radiative heat losses (Ω) evaluated with Equation (16) are negligible for all reactor geometries (Ω is equal to 0.03%, 0.22%, 0.50%, 0.00% and 1.11%, for the geometries A1), A2), A3), B) and C), respectively).

$$\Omega = \frac{q_{loss}}{a_V F_{cat/geo} \int_{L_{cat}} \sum_{k=1}^{KK_w} A\dot{\omega}_{k,w} H_k(x)dx} \times 100\% \quad (16)$$

Fig. 4a shows that along the front heat shield up to near the catalyst inlet section the surface temperatures of the diverging and converging conical-shaped reactors (geometries B) and C), respectively) are very similar to case studies A1) and A3), respectively. This is mainly due to similar flow velocities registered along the front heat shield. Fig. 4a and b also show that with a constant catalyst volume and length the converging conical-shaped reactor (case study C)) is more effective to decrease the surface temperatures in the catalyst region than the diverging configuration (case study B)). Among the five reactor geometries and for the operating condition considered, the geometries A3) and C) are the most adequate to guarantee a higher catalyst thermal stability because they allow a significant decrease on the maximum surface temperatures.

Fig. 5 presents the four steady-state contributive terms of the solid phase energy balance equation (Equation (4)). Heat conduction (diffusion) along the connected foam struts and heat convection between solid surfaces and the flowing gas mixture are the dominant modes of heat transfer. Fig. 5c shows for the cylindrical-shaped reactors (geometries A1), A2) and A3)) a decrease in the relative net heat release (source term) as the internal reactor diameter increases. This trend explains the decrease observed in Fig. 4a and b for the maximum surface temperatures. Fig. 5d reveals that radiative heat exchange between solid surfaces has a major importance near the interface between the front heat shield and the catalyst bed where sharp temperature gradients are well-known to exist (see Fig. 4a). Nevertheless, thermal radiation plays a minor role in the energy balance of the solid phase compared with the remaining heat transport modes.

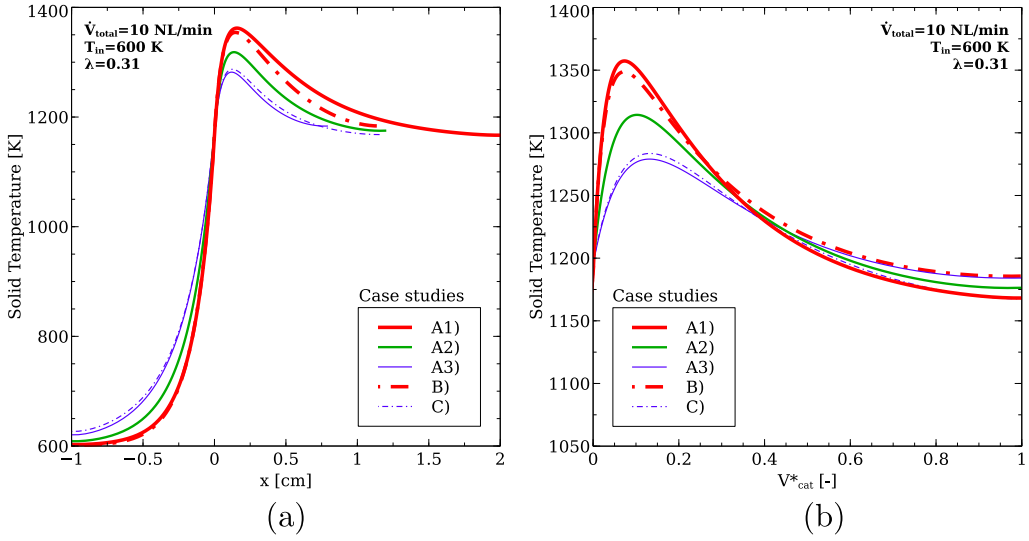

Fig. 4 – Surface temperature profiles for each case study: a) as a function of the axial reactor position; b) as a function of the dimensionless catalyst volume. Operating conditions: $\dot{V}_{total}$ = 10 NL/min; λ = 0.31; T_{in} = 600 K; P = 1 atm.

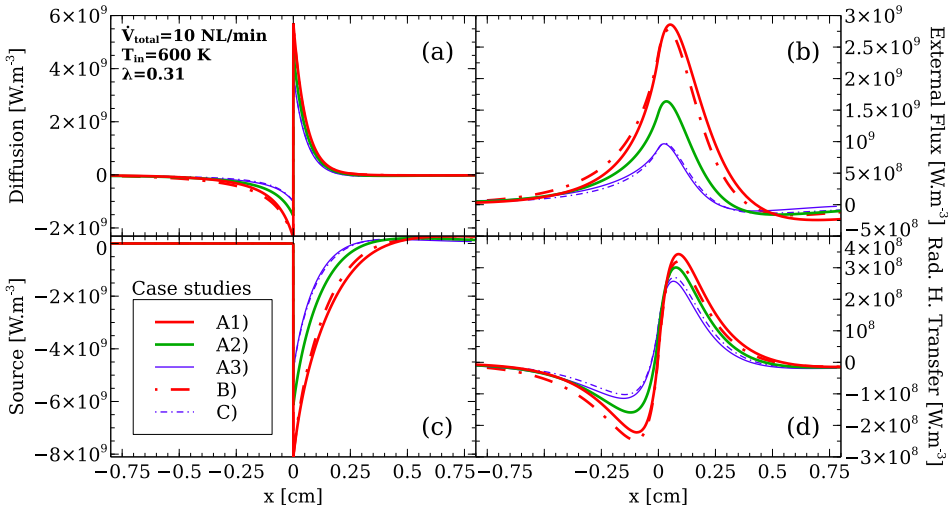

Fig. 5 – Terms of the solid phase energy balance equation: a) heat diffusion; b) interphase (external) heat flux; c) source; d) radiative heat transfer. Operating conditions: $\dot{V}_{total}$ = 10 NL/min; λ = 0.31; T_{in} = 600 K; P = 1 atm.

The effect of radiative heat transfer between solid walls on the surface temperature profiles for case studies A2), B) and C) can be observed in Fig. 6. The inclusion of the radiative heat transfer mode in the energy balance equation of the solid phase increases the surface temperatures along the front heat shield. This is due to the incoming net heat transfer fluxes from upstream hotter sections (see also Fig. 5d). As a consequence slightly lower surface temperatures are registered along the catalyst bed when thermal radiation is accounted for.

The weak influence played by thermal radiation on the energy balance of solid phase is mainly due to the thick radiative nature of the porous matrix. Fig. 5d shows that the radiative heat transfer becomes negligible in sections further downstream and upstream the catalyst entrance section because the porous media hinders the radiative heat exchange between interior reactor regions at high temperatures and regions at much lower surface temperatures located far upstream or downstream the former regions. Fig. 7a and b show for the reactor configurations B) and C), respectively, a set of five TEAs ($\overline{G_i G_j}$) between volume zones (g_i) centered in five specific axial locations and the remaining volume zones (g_j). The increase/decrease along the axial direction in $\overline{G_i G_i}$ values observed in Fig. 7a/b is due to the increase/decrease in the reactor cross-sectional area since the conservation constraints (summation laws) for the TEAs are respected. A rapid decay of the TEAs values is observed for volume zones near the hot spot region (x = 0.0 cm) justifying the thick radiative behavior of the cellular matrix. Foam monoliths with lower extinction coefficients would enhance the heat transfer rates by radiation between locations separated by longer axial distances. However, pursuing cellular structures with better radiative properties may lead to structures with worst geometrical properties to perform catalytic partial oxidation.

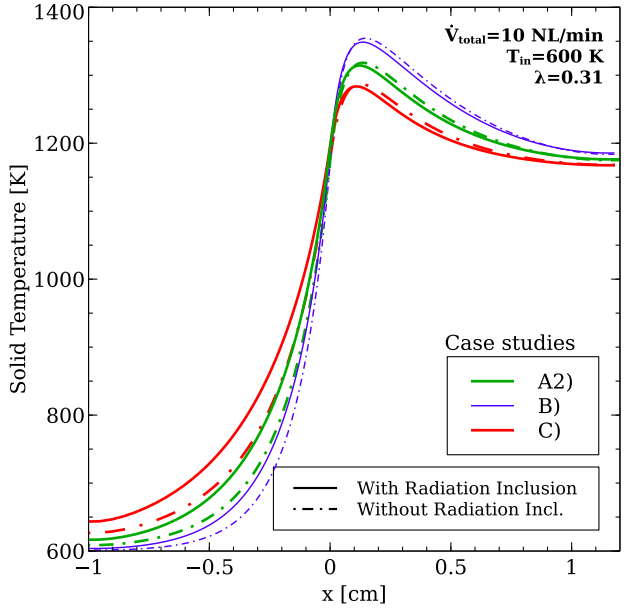

Fig. 6 – Solid thermal profiles with and without considering radiative heat transport in the solid phase energy balance. Operating conditions: $\dot{V}_{total}$ = 10 NL/min; λ = 0.31; T_{in} = 600 K; P = 1 atm.

The trends of the specific net heat release term observed in Fig. 5c are explained on the basis of reactants consumption rates. Fig. 8 presents the net molar production rates of oxygen and methane at the catalyst wall on a total reactor volume basis. O_2 consumption is strictly related to an overall positive heat release, namely through CH_4 (partial and total) oxidation reactions and deep oxidation reactions of H_2 and CO. Thereafter, the decrease observed before in the source term of the solid phase energy balance equation (see Fig. 5c) upon increasing the cross-sectional area of the cylindrical-shaped reactors is justified by a slower O_2 specific consumption rate, not only near the catalyst entrance section but also along the whole catalyst bed, as Fig. 8 shows. O_2 and CH_4 net molar consumption profiles of the diverging and converging conical-shaped reactors are very similar to those of the case studies A1) and A3), respectively, in particular near the hot spot region. These similar trends justify the similar temperature

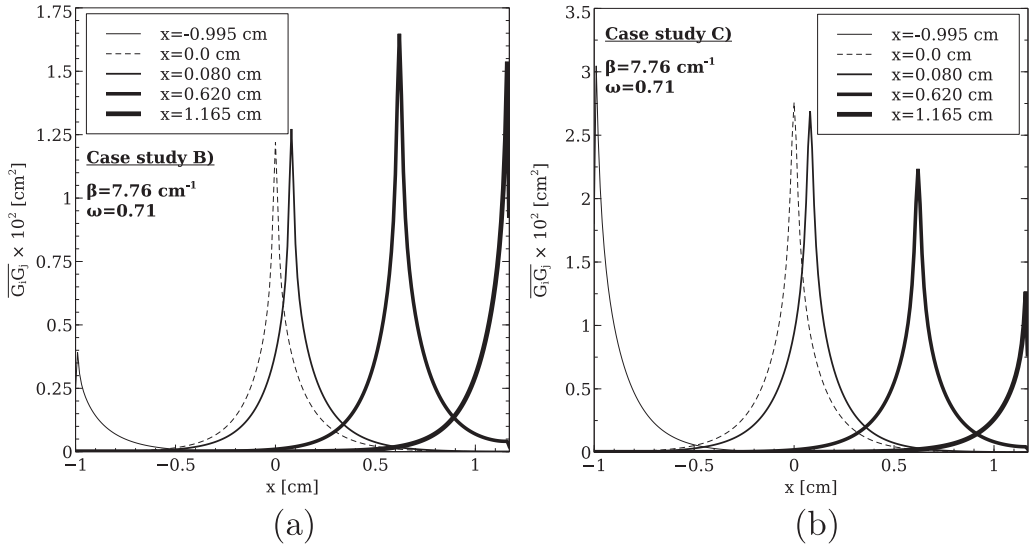

Fig. 7 – Total exchange areas between volume zones centered in specific axial locations and the remaining volume zones: a) case study B); b) case study C). Radiative properties: $\beta = 7.76\ cm^{-1}$; $\omega = 0.71$.

profiles near the catalyst inlet section observed before between case studies B) and A1) and C) and A3) (see Fig. 4 and b). Further downstream the hot spot region differences between such case studies in the $\dot{\omega}_{O_2}$ and $\dot{\omega}_{CH_4}$ profiles start to appear.

It is widely recognized that O_2 consumption during methane CPOx on Rh catalysts is fully governed by mass transport between the bulk gas flow and the catalyst surface (mass convection) [17,54]. Therefore, the rate of heat release due to O_2 consumption at the wall is controlled by the external mass transport of O_2. Fig. 9 presents the three steady-state terms of the O_2 mass balance equation (see Equation (1)). For a specific operating condition an increase in the reactor

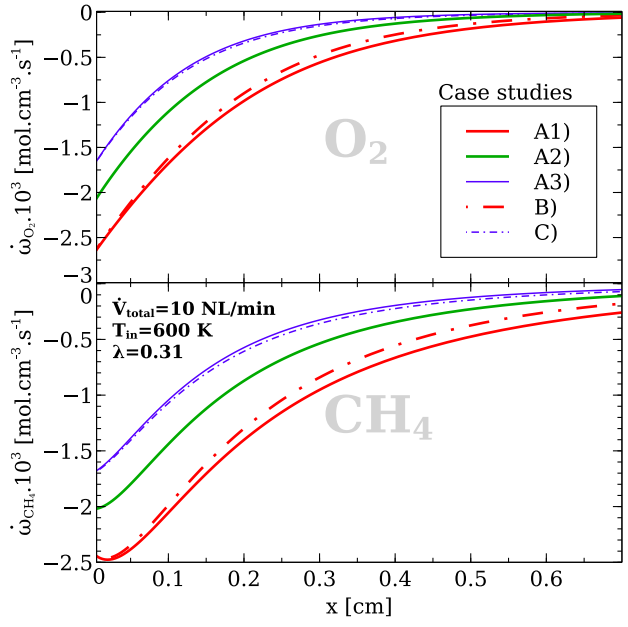

Fig. 8 – Specific net molar production rates of O_2 and CH_4 at the catalyst wall. Operating conditions: $\dot{V}_{total} = 10\ NL/min$; $\lambda = 0.31$; $T_{in} = 600\ K$; $P = 1\ atm$.

diameter leads to a general decrease in superficial flow velocities and consequently in the external transport rate of O_2 from the free flow to the external catalyst surface (see Fig. 9c). Once the rate of heat release at the catalyst wall is mainly dictated by the O_2 consumption rate, a decrease in the O_2 supply rate for surface reactions by a resistance in the external mass transport leads to a decrease in the net heat release and then to a decrease in surface temperatures since the heat transfer modes are more effective to flatten surface temperatures at lower values of specific net heat release. In Fig. 9 it is also noticeable that molecular diffusion starts to play an increasing role, namely near the catalyst inlet section, over the advection term as the reactor cross-sectional area is increased considering cylindrical-shaped reactors.

Besides lower superficial flow velocities that naturally conduct to a decrease in the external mass transport term as the reactor flow area is increased, the interphase mass transport coefficients ($K_{mat,k}$) also suffer a decrease due to a decrease of the *Re* number (see Equation (5)), derived from lower superficial flow velocities, contributing even more to a gas–solid diffusive limiting regime. Fig. 10 presents the external mass transport coefficients for CH_4 and O_2.

To prevent high surface temperatures a decrease in the O_2 external transport rate is highly beneficial in the oxidation zone. Case studies A3) and C) allow for the higher decrease in the external O_2 transport coefficients. In the reforming zone (downstream the oxidation zone – oxygen depleted region) the consumption of CH_4 through endothermic reforming reactions occurs in a mixed chemical/diffusive regime and allows for a decrease in the surface temperatures [17]. A slight increase in the local external CH_4 transport coefficients is observed for the case study C) in relation to the case study A3). As it will be shown this increase enhances the promotion of a higher fuel conversion and reforming efficiency in the case study C) than in case A3).

Beyond the catalyst thermal performance, highly informative for the catalyst thermal stability and ultimately for the

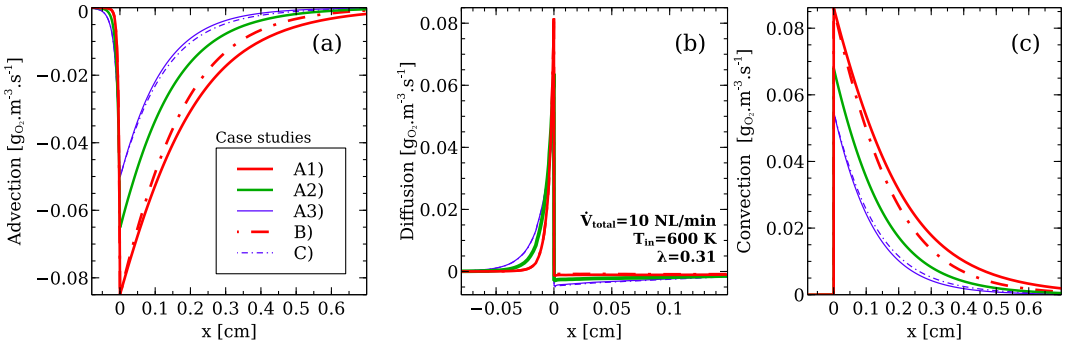

Fig. 9 – Terms of the gas phase species mass balance equation for O_2: a) advection; b) diffusion; c) interphase (external) mass flux. Operating conditions: $\dot{V}_{total}$ = 10 NL/min; λ = 0.31; T_{in} = 600 K; P = 1 atm.

catalyst durability, the catalyst reforming performance should also be evaluated and monitored in an attempt to improve the overall reforming process. The reactor reforming performance is commonly estimated through four reforming performance parameters, namely methane conversion (X_{CH_4}), H_2 and CO selectivities (S_{CO} and S_{H_2}) and reforming efficiency (η_{ref}). These parameters are evaluated for each reactor axial position, x, through the expressions that follows (Equations (17)–(20)).

$$X_{CH_4}(x) = \frac{(\dot{n}_{CH_4})_{in} - \dot{n}_{CH_4}(x)}{(\dot{n}_{CH_4})_{in}} \times 100\% \quad (17)$$

$$S_{H_2}(x) = \frac{\dot{n}_{H_2}(x)}{\dot{n}_{H_2}(x) + \dot{n}_{H_2O}(x)} \times 100\% \quad (18)$$

$$S_{CO}(x) = \frac{\dot{n}_{CO}(x)}{\dot{n}_{CO}(x) + \dot{n}_{CO_2}(x)} \times 100\% \quad (19)$$

$$\eta_{ref}(x) = \frac{\dot{n}_{H_2}(x)LHV_{H_2} + \dot{n}_{CO}(x)LHV_{CO}}{(\dot{n}_{CH_4})_{in}LHV_{CH_4}} \times 100\% \quad (20)$$

Fig. 11a shows the profiles of such performance parameters as a function of the reactor axial dimension whereas in Fig. 11b those profiles are plotted as a function of the non-dimensional catalyst volume. Fig. 11c shows the integral values for such performance parameters.

Fig. 11a shows that an increase in the cross-sectional area of cylindrical-shaped reactors allows to attain a higher methane conversion, H_2 selectivity and reforming efficiency in a lower axial reactor distance. At the axial position x = 0.79 cm (outlet section of the reactor assigned to the case study A3)) the case study A3) yields the highest values among all case studies for X_{CH_4}, S_{H_2} and η_{ref}.

The reforming performance parameters plotted against the dimensionless catalyst volume in Fig. 11b show that the case study A3) presents the lowest efficiency in the catalyst usage along the majority of the reactor, since with an equal catalyst volume the case study A3) provides the lowest values for methane conversion, hydrogen selectivity and reforming efficiency. A decrease in the reactor diameter (considering cylindrical-shaped reactors) allows for a higher catalyst reforming performance even though it requires a longer catalyst. Comparing the conical-shaped reactors (case studies B) and C)) with the cylindrical reactors having an equal catalyst inlet section diameter (case studies A1) and A3), respectively), case studies B) and C) present lower and higher values than case studies A1) and A3), respectively, for X_{CH_4}, S_{H_2} and η_{ref} along the catalyst bed as well as at the reactor outlet sections (see Fig. 11c). Moreover, the slightly higher gradients near the catalyst outlet section ($V^*_{cat} \approx 1.0$) presented by case study C) for methane conversion, hydrogen selectivity and reforming efficiency suggest that the integral differences observed between this case study and the remaining ones in Fig. 11c could be even more pronounced by considering a higher but constant catalyst volume for all case studies. For CO selectivity an inverse trend is registered, that is, case studies B) and C) present higher and lower values than case studies A1) and A3), respectively, even though the absolute difference is not meaningful for the total amount of catalyst considered. However, it should be noted that by increasing the total catalyst volume the differences in the reforming parameters should become more remarkable as the performance profiles observed in Fig. 11a and b may denounce.

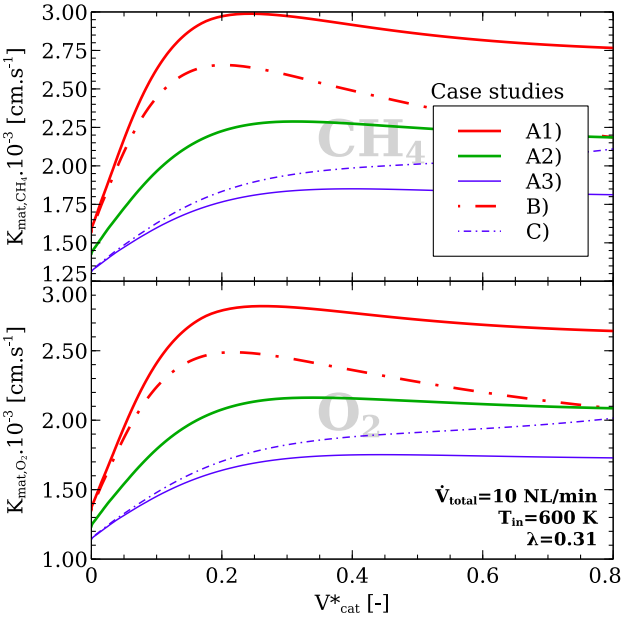

Fig. 10 – Interphase local mass transport coefficients of CH_4 and O_2 species. Operating conditions: $\dot{V}_{total}$ = 10 NL/min; λ = 0.31; T_{in} = 600 K; P = 1 atm.

Comparing case studies B) and C), as the reactor volume increases case study C) returns higher values for methane conversion, H_2 selectivity and reforming efficiency. Therefore, besides a worst thermal performance observed before for the diverging conical-shaped reactor (case study B)) this reactor geometry also collects a worst reforming performance than the converging conical-shaped reactor (case study C)).

The integration of a catalytic partial oxidation reactor in a specific system may require a low pressure drop value along the reforming reactor. In this work, the pressure drop in the reactor is estimated through the Forchheimer equation (Equation (21)) considering the empirical expressions for the viscous and inertial permeability parameters reported in Ref. [34].

$$\frac{\Delta P}{\Delta L} = \mu u \varepsilon \left(1.42 \times 10^{-4} D_p[m]^{1.18} \varepsilon^{7.00}\right)^{-1} + \rho_g (u\varepsilon)^2 \left(0.89 D_p[m]^{0.77} \varepsilon^{4.42}\right)^{-1} \quad (21)$$

Fig. 12 presents the total pressure drop values along the reactors for the five case studies. Case studies A1) and A3) register the highest and the lowest total pressure drop values among the reactor configurations considered. A decrease in the total pressure drop is observed as the cross-sectional area of the cylindrical-shaped reactors (case studies A1), A2) and A3)) is increased. The case study C) that has shown previously a significant better thermal performance than case study A1) and a similar reforming performance as the case study A1) takes once again advantage over the case study A1) regarding the pressure drop. The observed range for the pressure drop is well below 1% of the operating pressure (atmospheric pressure) which reinforces the irrelevance of the momentum balance equation in the mathematical model formulation for an accurate prediction of the reactor performance.

3.4. *Effect of flow rate*

The effect of the total flow rate on the five reactor configurations under consideration is herein analyzed with respect to the maximum surface temperatures and integral

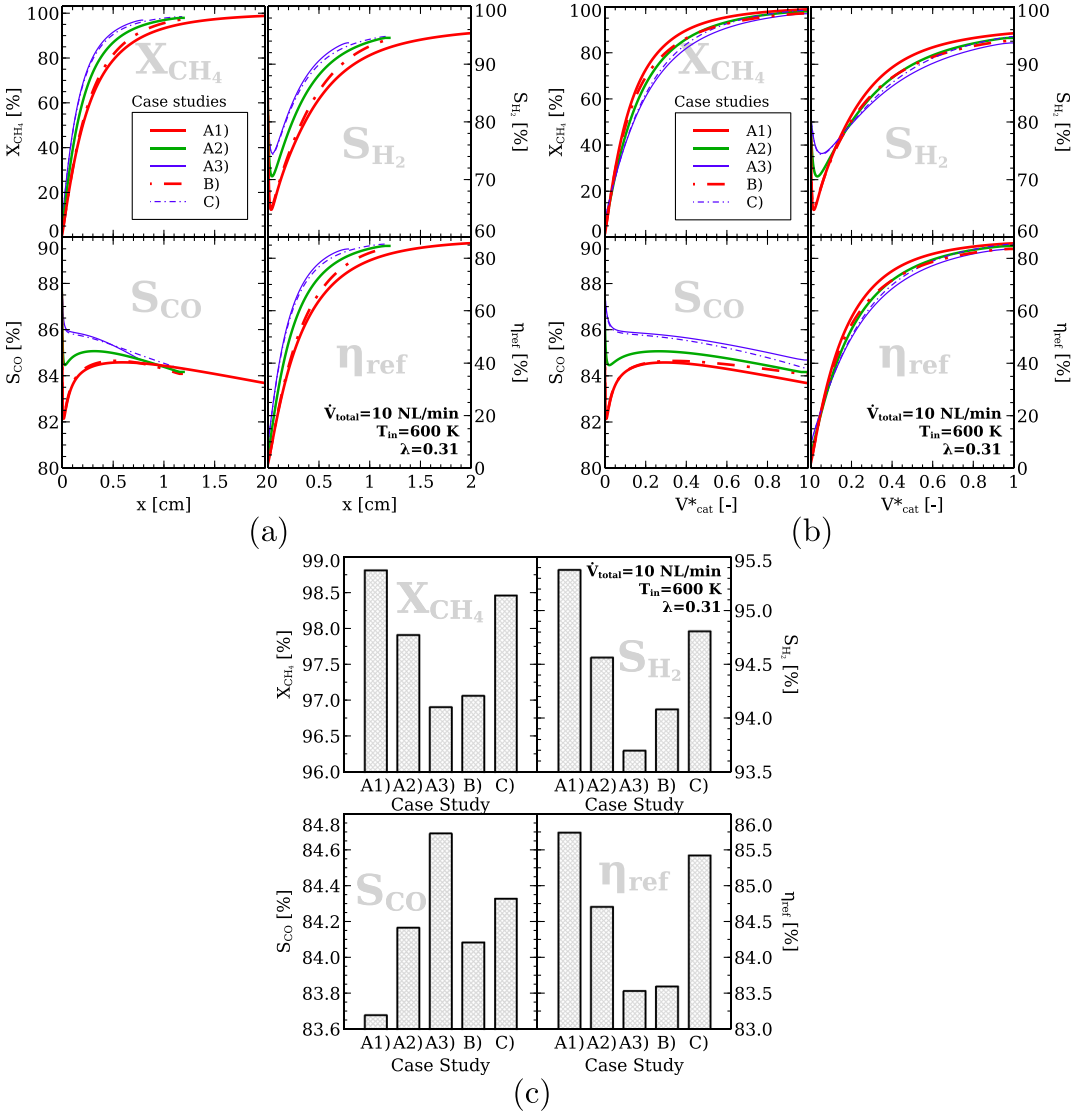

Fig. 11 – Methane conversion, H_2 and CO selectivities and reforming efficiency for each case study: a) as a function of the axial reactor position; b) as a function of the dimensionless catalyst volume; c) integral performance. Operating conditions: $\dot{V}_{total}$ = 10 NL/min; λ = 0.31; T_{in} = 600 K; P = 1 atm.

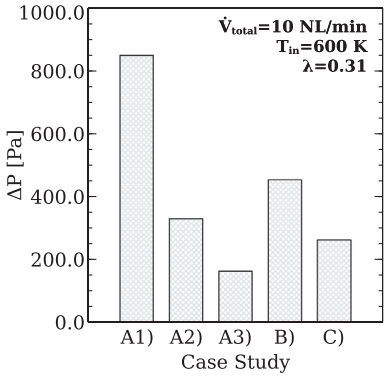

Fig. 12 – Pressure drop in the reactor for each case study. Operating conditions: $\dot{V}_{total}=10$ **NL/min**; $\lambda=0.31$; $T_{in}=600$ **K**; **P=1 atm.**

reforming performance. Different total flow rate values (2, 5, 10 and 15 NL/min) are considered along with the operating pressure, inlet mixture composition and preheating temperature defined in the previous section. Fig. 13a presents the maximum solid temperatures whereas the fuel conversion, syngas selectivities and reforming efficiency at the reactor outlet section for each case study are presented in Fig. 13b.

As expected for each reactor geometry upon increasing the flow rate the maximum surface temperatures also increase. Considering the cylindrical-shaped reactors similar conclusions to those drawn previously (for 10 NL/min) are observed in Fig. 13a for each flow rate that is $T_{s,max}^{A1)} > T_{s,max}^{A2)} > T_{s,max}^{A3)}$. As the flow rate decreases the converging conical-shaped reactor (case study C)) gains a slight advantage over the case study A3) to decrease the maximum surface temperature. The absolute differences between the maximum surface temperatures observed in cases B) and A1) decrease as the flow rate decreases.

Fig. 13b shows that the case study A1) is the most adequate to achieve the highest values for methane conversion, hydrogen selectivity and reforming efficiency from moderate to high flow rates but it leads to a prohibitive thermal behavior concerning the catalyst thermal stability. On the contrary, for the same range of operating conditions the converging conical-shaped reactor (case study C)) allows for lower surface temperatures with methane conversion and reforming efficiency values very near to those obtained through the case study A1). Case studies C) and A3) have similar maximum surface temperatures however case study C) allows to obtain higher values for methane conversion and reforming efficiency than case A3).

For low flow rates the catalyst thermal stability is not a key issue considering that the catalyst was designed for operating with higher input thermal loads. At low flow rates performing partial oxidation with a high reforming performance is the key challenge. Concerning the cylindrical case studies, Fig. 13b shows that decreasing the flow rate the difference in fuel conversion and reforming efficiency values registered between case studies A2)/A3) with A1) becomes lower. Moreover, at very low flow rates the reforming efficiency values registered for the case study A2) is higher than that of case study A1, mainly due to the promotion of CO selectivity observed for the case study A2).

Increasing the total flow rate for each case study the total pressure drop also increases. Although not shown, the highest pressure drop value was observed for the case study A1) at the highest total flow rate value being about 1283 Pa (~1.3% of the operating pressure).

4. Conclusions

The effect of the reactor geometry on the performance of methane catalytic partial oxidation was numerically evaluated. The performance of the cylindrical reactor geometry was

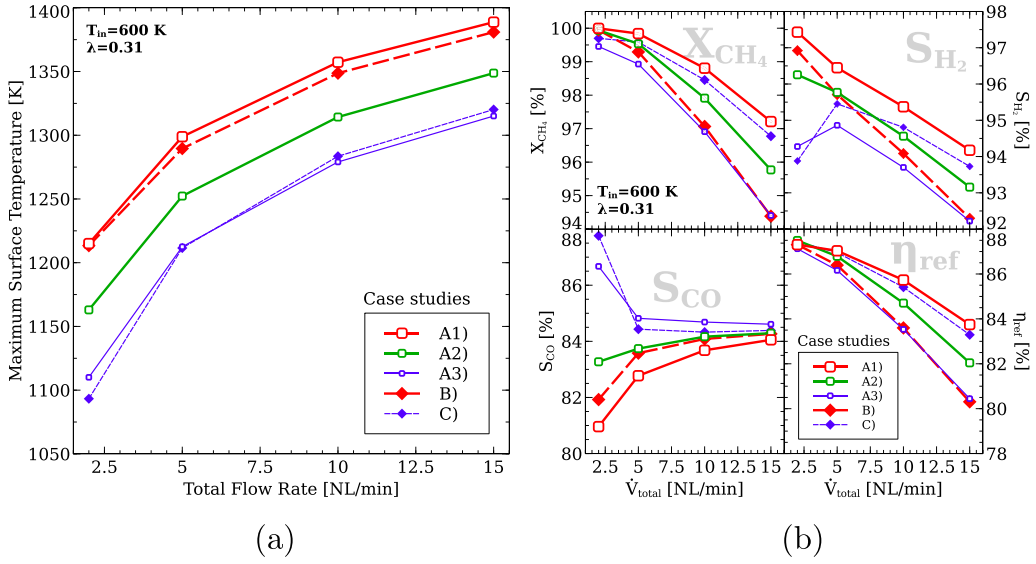

Fig. 13 – Role of the total flow rate on the performance of the different reactor geometries: a) maximum surface temperatures; b) integral values of methane conversion, H_2 and CO selectivities and reforming efficiency. Operating conditions: $\dot{V}_{total}=\{2;5;10;15\}$ **NL/min**; $\lambda=0.31$; $T_{in}=600$ **K**; **P=1 atm.**

compared with the performance of diverging and converging conical-shaped reactors having an equal catalyst volume. Foam monoliths were regarded as the catalyst support structures in this study. A 1D two-phase mathematical model for fixed bed reactors was employed. The model allows for a variable reactor cross-sectional area along the main flow direction and accounts for detailed surface kinetics and radiative heat transfer in the porous matrix.

Catalyst thermal stability and reforming performance were considered key parameters during the current investigation. If catalyst thermal stability is the most important issue during reactor operation then reactor configurations that lead to lower surface temperatures would be preferable. For cylindrical-shaped reactors the maximum surface temperature is decreased by increasing the reactor cross-sectional area. However, through an increase in the internal reactor diameter a significant decrease in the fuel conversion and reforming efficiency was registered. Another strategy to accomplish a significant surface temperature decrease in such a way that catalyst stability is improved was herein investigated by considering conical-shaped reactors. In particular, converging conical-shaped reactors were proposed to efficiently decrease the hot spot temperature yielding at the same time high fuel conversion, high reforming efficiency and low total pressure drop over a broad range of fuel flow rates. On the other hand, by considering a diverging conical-shaped reactor lower thermal advantages and reforming performance were observed.

The registered surface temperature decrease was attributed to an increase in the external transport resistance of O_2 from the bulk gas stream to the catalyst surface. The specific O_2 consumption rate is directly related to the net heat release through the oxidation reactions.

Acknowledgments

This work was partially financed by the European Commission within the 7th Framework Program (260105 FC-DISTRICT).

REFERENCES

[1] Hickman DA, Schmidt LD. Synthesis gas formation by direct oxidation of methane over Pt monoliths. J Catal 1992;138:267–82.
[2] Hickman DA, Haupfear EA, Schmidt LD. Synthesis gas formation by direct oxidation of methane over Rh monoliths. Catal Lett 1993;17:223–37.
[3] York APE, Xiao T, Green MLH. Brief overview of the partial oxidation of methane to synthesis gas. Top Catal 2003;22:345–58.
[4] Nematollahi B, Rezaei M, Khajenoori M. Combined dry reforming and partial oxidation of methane to synthesis gas on noble metal catalysts. Int J Hydrogen Energy 2011;36:2969–78.
[5] Claridge JB, Green MLH, Tsang SC, York APE, Ashcroft AT, Battle PD. A study of carbon deposition on catalysts during the partial oxidation of methane to synthesis gas. Catal Lett 1993;22:299–305.
[6] Barrio VL, Schaub G, Rohde M, Rabe S, Vogel F, Cambra JF, et al. Reactor modeling to simulate catalytic partial oxidation and steam reforming of methane. Comparison of temperature profiles and strategies for hot spot minimization. Int J Hydrogen Energy 2007;32:1421–8.
[7] Tavazzi I, Maestri M, Beretta A, Groppi G, Tronconi E, Forzatti P. Steady-state and transient analysis of a CH_4-catalytic partial oxidation reformer. AIChE J 2006;52:3234–45.
[8] Dalle Nogare D, Degenstein NJ, Horn R, Canu P, Schmidt LD. Modeling spatially resolved data of methane catalytic partial oxidation on Rh foam catalyst at different inlet compositions and flowrates. J Catal 2011;277:134–48.
[9] Schwiedernoch R, Tischer S, Correa C, Deutschmann O. Experimental and numerical study on the transient behavior of partial oxidation of methane in a catalytic monolith. Chem Eng Sci 2003;58:633–42.
[10] Chen J, Yang H, Wang N, Ring Z, Dabros T. Mathematical modeling of monolith catalysts and reactors for gas phase reactions. Appli Catal A Gen 2008;345:1–11.
[11] Hickman DA, Schmidt LD. Steps in CH_4 oxidation on Pt and Rh surfaces: high-temperature reactor simulations. AIChE J 1993;39:1164–77.
[12] Deutschmann O, Schmidt LD. Modeling the partial oxidation of methane in a short-contact-time reactor. AIChE J 1998;44(11):2465–77.
[13] Tavazzi I, Beretta A, Groppi G, Forzatti P. Development of a molecular kinetic scheme for methane partial oxidation over Rh/α-Al_2O_3 catalyst. J Catal 2006;241:1–13.
[14] Donazzi A, Beretta A, Groppi G, Forzatti P. Catalytic partial oxidation of methane over a 4% Rh/α-Al_2O_3 catalyst. Part I: kinetic study in annular reactor. J Catal 2008;255:241–58.
[15] Mhadeshwar AB, Vlachos DG. Hierarchical multiscale mechanism development for methane partial oxidation and reforming and for thermal decomposition of oxygenates on Rh. J Phys Chem B 2005;109:16819–35.
[16] Maestri M, Vlachos DG, Beretta A, Groppi G, Tronconi E. A C1 microkinetic model for methane conversion to syngas on Rh/α-Al_2O_3. AIChE J 2009;55:993–1008.
[17] Beretta A, Groppi G, Lualdi M, Tavazzi I, Forzatti P. Experimental and modeling analysis of methane partial oxidation: transient and steady-state behavior of Rh-coated honeycomb monoliths. Ind Eng Chem Res 2009;48:3825–36.
[18] Beretta A, Donazzi A, Livio D, Maestri M, Groppi G, Tronconi E, et al. Optimal design of a CH_4 CPO-reformer with honeycomb catalyst: combined effect of catalyst load and channel size on the surface temperature profile. Catal Today 2011;171:79–83.
[19] Scognamiglio D, Russo L, Maffettone PL, Salemme L, Simeone M, Crescitelli S. Modelling and simulation of a catalytic autothermal methane reformer with Rh catalyst. Int J Hydrogen Energy 2012;37:263–75.
[20] Bizzi M, Saracco G, Schwiedernoch R, Deutschmann O. Modeling the partial oxidation of methane in a fixed bed with detailed chemistry. AIChE J 2004;50:1289–99.
[21] Forzatti P, Groppi G. Catalytic combustion for the production of energy. Catal Today 1999;54:165–80.
[22] Tavazzi I, Beretta A, Groppi G, Maestri M, Tronconi E, Forzatti P. Experimental and modeling analysis of the effect of catalyst aging on the performance of a short contact time adiabatic CH_4-CPO reactor. Catal Today 2007;129:372–9.
[23] Ding S, Yang Y, Jin Y, Cheng Y. Catalyst deactivation of Rh-coated foam monolith for catalytic partial oxidation of methane. Ind Eng Chem Res 2009;48:2878–85.
[24] Donazzi A, Maestri M, Beretta A, Groppi G, Tronconi E, Forzatti P. Microkinetic analysis of CH_4 CPO tests with CO_2-diluted feed streams. Appl Catal A 2011;391:350–9.
[25] Ding S, Wu C, Cheng Y, Jin Y, Cheng Y. Analysis of catalytic partial oxidation of methane on rhodium-coated foam

monolith using CFD with detailed chemistry. Chem Eng Sci 2010;65:1989–99.
[26] Wen C, Liu Y, Guo Y, Wang Y, Lu G. Strategy to eliminate catalyst hot-spots in the partial oxidation of methane: enhancing its activity for direct hydrogen production by reducing the reactivity of lattice oxygen. Chem Commun 2010;46:880–2.
[27] Livio D, Donazzi A, Beretta A, Groppi G, Forzatti P. Optimal design of a CPO-reformer of light hydrocarbons with honeycomb catalyst: effect of frontal heat dispersions on the temperature profiles. Top Catal 2011;54:866–72.
[28] Navalho JEP, Frenzel I, Loukou A, Pereira JMC, Trimis D, Pereira JCF. Catalytic partial oxidation of methane rich mixtures in non-adiabatic monolith reactors. Int J Hydrogen Energy 2013;38:6989–7006.
[29] Dashliborun AM, Fatemi S, Najafabadi AT. Hydrogen production through partial oxidation of methane in a new reactor configuration. Int J Hydrogen Energy 2013;38:1901–9.
[30] Hüppmeier J, Barg S, Baune M, Koch D, Grathwohl G, Thöming J. Oxygen feed membranes in autothermal steam-reformers - a robust temperature control. Fuel 2010;89:1257–64.
[31] Rodríguez ML, Pedernera MN, Borio DO. Two dimensional modeling of a membrane reactor for ATR of methane. Catal Today 2012;193:137–44.
[32] Kumar S, Kumar S, Prajapati JK. Hydrogen production by partial oxidation of methane: modeling and simulation. Int J Hydrogen Energy 2009;34:6655–68.
[33] Munro RG. Evaluated material properties for a sintered α–alumina. J Am Ceram Soc 1997;80:1919–28.
[34] Garrido GI, Patcas FC, Lang S, Kraushaar-Czarnetzki B. Mass transfer and pressure drop in ceramic foams: a description for different pore sizes and porosities. Chem Eng Sci 2008;63:5202–17.
[35] Fourie JG, Du Plessis JP. Effective and coupled thermal conductivities of isotropic open-cellular foams. AIChE J 2004;50:547–56.
[36] Parthasarathy P, Habisreuther P, Zarzalis N. Identification of radiative properties of reticulated ceramic porous inert media using ray tracing technique. J Quant Spectrosc Radiat Transf 2012;113:1961–9.
[37] Navalho JEP, Pereira JMC, Ervilha AR, Pereira JCF. Uncertainty quantification in the catalytic partial oxidation of methane. Combust Theory Model 2013;17:1067–95.
[38] Poinsot T, Veynante D. Theoretical and numerical combustion. Philadelphia, USA: R. T. Edwards; 2005.
[39] Deutschmann O, Schwiedernoch R, Maier LI, Chatterjee D. Natural gas conversion in monolithic catalysts: interaction of chemical reactions and transport phenomena. Stud Surf Sci Catal 2001;136:251–8.
[40] Hartmann M, Maier L, Minh HD, Deutschmann O. Catalytic partial oxidation of iso-octane over rhodium catalysts: an experimental, modeling, and simulation study. Combust Flame 2010;157:1771–82.
[41] Eriksson S, Schneider A, Mantzaras J, Wolf M, Järås S. Experimental and numerical investigation of supported rhodium catalysts for partial oxidation of methane in exhaust gas diluted reaction mixtures. Chem Eng Sci 2007;62:3991–4011.
[42] Donazzi A, Maestri M, Michael BC, Beretta A, Forzatti P, Groppi G, et al. Microkinetic modeling of spatially resolved autothermal CH_4 catalytic partial oxidation experiments over Rh-coated foams. J Catal 2010;275:270–9.
[43] Mazumder S, Grimm M. Numerical investigation of radiation effects in monolithic catalytic combustion reactors. Int J Chem Reactor Eng 2011;9.
[44] Modest MF. Radiative heat transfer. New York: McGraw-Hill; 1993.
[45] Larsen ME, Howell JR. Least-squares smoothing of direct-exchange areas in zonal analysis. J Heat Transf 1986;108:239–42.
[46] Naraghi MHN, Chung BTF. A unified matrix formulation for the zone method: a stochastic approach. Int J Heat Mass Transf 1985;28(1):245–51.
[47] Kee RJ, Grcar JF, Smooke MD, Miller JA. Premix: a Fortran program for modeling steady laminar one-dimensional premixed flames. Tech. Rep. SAND85–8240. Sandia National Laboratories; 1985.
[48] Kee RJ, Rubley FM, Meeks E. CHEMKIN-II: a Fortran chemical kinetic package for the analysis of gas-phase chemical kinetics. Tech. Rep. SAND89–8009. Sandia National Laboratories; 1989.
[49] Kee RJ, Dixon-Lewis G, Warnatz J, Coltrin ME, Miller JA. A Fortran computer code package for the evaluation of gas-phase multicomponent transport properties. Tech. Rep. SAND86–8246. Sandia National Laboratories; 1986.
[50] Smith GP, Golden DM, Frenklach M, Moriarty NW, Eiteneer B, Goldenberg M., et al. GRI-Mech 3.0. http://www.me.berkeley.edu/gri_mech/.
[51] Hunter B, Guo Z. Comparison of the discrete-ordinates method and the finite-volume method for steady-state and ultrafast radiative transfer analysis in cylindrical coordinates. Numer Heat Transf Part B 2011;59:339–59.
[52] Kim MY. Assessment of the axisymmetric radiative heat transfer in a cylindrical enclosure with the finite volume method. Int J Heat Mass Transf 2008;51:5144–53.
[53] Kim MY, Baek SW. Modeling of radiative heat transfer in an axisymmetric cylindrical enclosure with participating medium. J Quant Spectrosc Radiat Transf 2005;90:377–88.
[54] Horn R, Williams KA, Degenstein NJ, Bitsch-Larsen A, Dalle Nogare D, Tupy SA, et al. Methane catalytic partial oxidation on autothermal Rh and Pt foam catalysts: oxidation and reforming zones, transport effects, and approach to thermodynamic equilibrium. J Catal 2007;249:380–93.